

Origin of stray grain formation in single-crystal superalloy weld pools from heat transfer and fluid flow modeling

T.D. Anderson^a, J.N. DuPont^{a,*}, T. DebRoy^b

^a Department of Materials Science and Engineering, Lehigh University, Bethlehem, PA 18015, USA

^b Department of Materials Science and Engineering, The Pennsylvania State University, University Park, PA 16802, USA

Received 28 May 2009; received in revised form 21 September 2009; accepted 26 October 2009

Available online 5 December 2009

Abstract

Stray grain formation in laser and electron beam welds on single-crystal alloy CMSX-4 was investigated through heat transfer and fluid flow simulations. The results were combined with a single-crystal growth model and stray grain calculations to investigate the influence of welding parameters on stray grain formation. Stray grain contents were also experimentally measured on laser and electron beam welds prepared over a wide range of parameters. The experimental and simulation results each demonstrate that stray grain content initially increases and then decreases with increasing travel speed. Increases in beam power produce an increase in the stray grain content. The results also demonstrate that restriction of growth along $\langle 1\ 0\ 0 \rangle$ directions decreases the magnitude of the temperature gradient and increases the growth rate along the dendrite growth direction (relative to the solidification interface normal). This effect promotes stray grain formation in the pool by increasing the extent of constitutional supercooling.

© 2009 Acta Materialia Inc. Published by Elsevier Ltd. All rights reserved.

Keywords: Single crystal; Weld repair; Constitutional supercooling; Stray grain formation

1. Introduction

The efficiency of a gas turbine engine is reliant on the ability of the engine to operate at high temperatures. Nickel-base superalloys have long been employed by the aerospace and energy industries in this application for their superior strength and fracture resistance at elevated temperatures. The excellent high-temperature mechanical properties are the result of precipitation of the ordered γ' phase, and the effects of creep deformation have been reduced through the use of a monocrystalline structure [1]. While these single-crystal (SX) casting techniques impart superior performance, the process itself is very expensive. A typical SX gas turbine blade can cost as much as \$30,000 to manufacture [2]. While the overall benefits justify the initial cost, several failure mechanisms can adversely affect the lifetime of a blade in service. Mechan-

ical surface wear, erosion of the blade tip, thermal fatigue cracking and hot corrosion [3] can lead to reduced performance, and will eventually require removal of the blade from service. In addition, crystalline imperfections resulting from the casting process can also disqualify the blade from service. Currently, techniques for repairing a failed or miscast SX component are not always reproducible, so the blades are often discarded. An effective method for repairing a damage or miscast blade could result in significant cost savings in the gas turbine industry. Much research has focused on the use of a weld repair method for this purpose. The primary challenge to successful weld repairs is the maintenance of the SX microstructure in the repair area.

When solidifying weld metal grows epitaxially from the SX substrate, the crystallographic orientation of the base and weld metals will be continuous, and growth will occur along one of the “easy” crystal directions (for cubic metals). However, certain conditions may arise in the weld pool that promote the nucleation and growth of equiaxed

* Corresponding author. Tel.: +1 610 758 3942; fax: +1 610 758 4244.
E-mail address: Jnd1@lehigh.edu (J.N. DuPont).

grains in the liquid which will have a crystallographic orientation independent from the substrate. Much research has been devoted towards understanding this columnar-to-equiaxed transition (CET). Initially described by Hunt [4] for casting processes, the CET is caused by excessive constitutional supercooling (CS). The amount of CS is usually defined by the value G/V (where G = thermal gradient and V = solidification velocity), wherein a lower G/V leads to more CS. When the amount of liquid undercooling surpasses the required undercooling for nucleation (ΔT_N), it becomes possible for equiaxed grains to nucleate ahead of the columnar dendrites. Because the crystallographic orientation of these equiaxed grains strays from that of the base metal, these equiaxed crystals are often termed “stray” grains (SGs). Unlike casting, a wide range of G and V will be present across the solidifying front in a weld pool. In addition, the restriction on epitaxial growth directions imparted by the SX substrate further alters the distribution of G and V . The relevant values parallel to the dendrite axes, G_{hkl} and V_{hkl} , are accurately described by the geometric model developed by Rappaz et al. [5–7]. The model asserts that the growth rate will be a function of the heat source travel speed V_b and the weld pool shape according to the equation:

$$|V_{hkl}| = |V_b| \frac{\cos \theta}{\cos \psi} \quad (1)$$

where θ is the angle between the normal to the solidification interface and welding velocity and ψ is the angle between the normal to the solidification interface and the growth direction. The $\langle 100 \rangle$ vector which is locally operative is that which is mostly closely aligned with the solidification interface normal vector. The orientation of the heat source motion with respect to the substrate surface orientation is thus a strong factor in the final crystal configuration in the weld zone. The shape of the weld pool, however, has been shown to be independent of orientation for cubic crystals [6], since heat conduction is isotropic. Hunt’s model of the CET in casting processes also described the importance of the alloy composition, particularly its effect on nucleation processes. The nucleation undercooling ΔT_N was mentioned previously, but composition will also control the nucleation density N_o . A higher N_o introduces more eligible sites for SGs to nucleate and grow.

Gaumann et al. [8] extended Hunt’s model to a wider range of solidification conditions by incorporating them within the Kurz–Giovanola–Trivedi (KGT) model for rapid solidification. That work developed models which enabled prediction of the type of solidification (SX vs. polycrystalline, PX) as a function of G and V . A more direct continuation of Hunt’s work was produced later, wherein his equations were further developed and applied for the case of welding processes [9], giving:

$$\frac{G^n}{V} = a \left\{ \sqrt[3]{\frac{-4\pi N_o}{3 \ln[1 - \phi]}} \cdot \frac{1}{n+1} \right\}^n \quad (2)$$

where a and n are material constants and N_o is the nuclei density. The two models are shown relative to one another in Fig. 1. Hunt’s model assumes that liquid undercooling will be negligible under the high- G conditions present during laser welding. To approximate the conditions of the CET, it is assumed that ϕ values below 0.0066 have a negligible effect on SX growth so that the CET does not occur below this value. The nucleation density was approximated using SG measurements from a series of laser weld trials. Since the right-hand side of the equations consists entirely of constants, a CET will occur when:

$$\frac{G^{3.4}}{V} < 2.7 \times 10^{24} \text{ (K}^{3.4}/\text{m}^{4.4} \text{ s)} \quad (3)$$

It is important to note that G and V are a strong function of position within the melt pool. Gaumann proposed using a depth-weighted average of G^n/V to characterize a single weld pool. The difficulty in comparing this model with experimental welds lies in the wide range of G and V present along the solidification interface.

Vitek [10] avoided this simplification by using the model to directly calculate ϕ along all points of a simulated weld pool. The pool shapes and temperature gradients were calculated using the Rosenthal equation [11], and the outputted pool shape and temperature fields were used to determine the local values of ϕ . The area-weighted average of ϕ was then used to characterize the SG formation behavior for a single set of welding conditions. The results of that work illustrated the effects of a wide range of processing parameters (beam power, travel speed, substrate crystal orientation) which accurately described the limited experimental results available.

Yoshihiro et al. [12] recently investigated the microstructure of welds on Alloy CMSX-4 prepared over a wide range of powers and travel speeds using both the laser and gas tungsten arc (GTA) heat sources. They identified three types of morphologies: single crystals with directional dendrites that only grow in the $[001]$ direction from the bottom of the weld, single crystals with disoriented dendrites, and welds

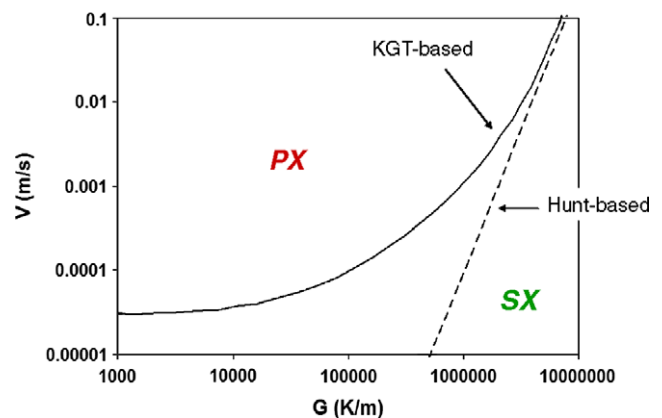


Fig. 1. Gaumann’s models of the CET boundary for superalloy CMSX-4 as a function of solidification parameters G and V : (a) KGT-based model for directional solidification and (b) original Hunt-based model.

with SGs. The SX welds with disoriented dendrites simply indicate the presence of dendrites that grew in directions orthogonal to the $[0\ 0\ 1]$ direction. Their results generally demonstrated that a reduction in power and increase in travel speed is beneficial for preserving the SX structure. The successful processing window for the GTA welds was slightly smaller than that for the laser welds. This is probably associated with the higher intensity heat source of the laser, which produces a higher temperature gradient.

The substrate orientation relative to the direction of the heat source travel speed can also influence the formation of SGs. For relatively simple conditions in which the direction of the heat source travel is coincident with one of the crystallographic $\langle 1\ 0\ 0 \rangle$ easy growth directions, the dendrite growth velocities across the line of symmetry in the fusion zone are equivalent. As a result, the tendency for SG formation is symmetrical about the weld centerline. There are likely to be conditions in which welding is required in an asymmetrical direction relative to the easy growth directions. Park et al. investigated this effect on welds of SX alloy Rene N5 alloy [13] and demonstrated that the SG formation tendency will be different on each half of the weld for this condition. This effect is caused by differences in the growth angle and associated growth velocity across the weld centerline that occur due to the asymmetric welding condition. In addition, the temperature gradient in the direction of dendrite growth will decrease as the growth angle increases. Therefore, the G/V ratio will be different on each side of the weld. Park et al. showed that conditions can exist in which the critical G/V ratio required to reach the CET is obtained on one side of the weld, while the G/V ratio on the other side is high enough to generally avoid the CET.

Additional research by the same group [14] has demonstrated that the cooling rate (product of GV) is symmetrical across the weld centerline. This carries important implications for identifying the mechanism of the CET. It is thought that the CET could also be induced by fragmented dendrites that are pushed into the solidification front by convection. Such dendrites would induce the CET by forming heterogeneous nucleation sites. In this case, convection would become more prevalent as GV decreases, and a decrease in cooling rate would therefore be expected to lead to more SGs. The value of GV was shown to be constant across the fusion line for the experimental welds examined, but the extent of SG formation is not. Therefore, the dendrite fragmentation mechanism is not likely to be operable in fusion welding.

Liu and DuPont [15,16] recently extended the analysis of Rappaz by combining Eq. (1) with a mathematical model of the melt pool. The three-dimensional (3-D) shape of the melt pool was modeled as the segment of an ellipsoid and represented by four geometrical parameters. The melt pool geometrical parameters are controlled by the heat and fluid flow conditions during processing and can be determined either computationally from a heat and fluid flow simulation or experimentally by directly measuring these parameters in situ or after processing. Coupling of this

3-D melt pool model to the dendrite growth analysis represented by Eq. (1) permitted detailed investigations of the effects of both melt pool shape and substrate orientation on the dendrite growth directions and velocities. A comparison of experimental and calculated dendrite growth directions were made, and good agreement was observed.

The results showed that the pool shape has a significant effect on the operable dendrite growth direction and resultant velocity. When the weld is relatively deep, growth is generally activated in four $\langle 1\ 0\ 0 \rangle$ type directions. Dendrites grow from the bottom of the pool in the $[0\ 0\ 1]$ direction, from the sides of the pool in the $[0\ 1\ 0]$ and $[0\ \bar{1}\ 0]$ directions, and from the back of the pool (along the heat source travel direction) in the $[1\ 0\ 0]$ direction. The favored growth along the $[1\ 0\ 0]$ direction that is coincident with the heat source direction causes the maximum growth velocity to equal that of the heat source velocity in this location. When the weld is shallow, growth generally occurs from the bottom of the pool, and the maximum growth velocity is generally less than the heat source velocity. Under asymmetrical welding conditions, the dendrite growth velocity can reach values that are up to 1.4 times that of the heat source velocity near the top of the pool.

Successful repair of SX alloys requires both a general understanding of the influence of processing conditions on SG formation as well as a predictive tool to aid in identifying process parameters that will avoid/minimize the occurrence of SGs. The formation of solidification cracks within the repair area also needs to be avoided. The general effects of welding parameters, substrate orientation and welding process type on the development of SGs over a wide range of conditions has been described in a companion paper along with the formation of different types of SGs that were observed experimentally [17]. Selected results from a heat/fluid flow and solidification model were used to help develop a detailed understanding of these effects. The influence of welding parameters on solidification cracking susceptibility has also been investigated [18]. In that work, it was observed that solidification cracking susceptibility can be minimized by utilizing low heat input welding conditions. For the conditions considered, process maps were developed for producing crack-free welds with both the gas tungsten arc and laser welding processes. The successful processing window was larger for the laser process. This was attributed to the higher temperature gradient associated with the laser process, which helps minimize SGs and the associated formation of solidification cracks that form along the grain boundaries. The development and application of heat/fluid flow and solidification modeling techniques for predicting SG formation in welds is described in this paper. The work presented here seeks to improve upon research conducted to date by utilizing a more advanced method for weld pool simulation that accounts for both heat and fluid flow, and validating the calculated results using data from a large number of experimental weld trials. The heat/fluid flow model was first validated for prediction of the melt pool shape and

variation in temperature gradient around the melt pool. The heat/fluid flow results are then integrated into a solidification model for determining the active growth directions as well as the temperature gradient and solidification velocity along the dendrite growth direction as an aid to predicting conditions that lead to the formation of SGs.

2. Procedure

2.1. Modeling

Weld pool simulations were carried out using the heat transfer and fluid flow code developed by DebRoy et al. [19,20]. Temperature and fluid velocity fields are calculated using fundamental equations of conservation of mass, momentum and energy with appropriate boundary conditions. Being a 3-D finite-difference code, the calculations require the design of a mesh upon which they are performed. A unique mesh was designed for each set of welding parameters in order to obtain good resolution of variables within the simulated melt pool. Using the assumption that weld pools are symmetric about their centerline, only one-half of the melt pool was simulated. The entirety of the mesh occupied dimensions of $3.3 \times 0.5 \times 0.6$ cm, although the mesh was refined in the locality of the melt pool. While the boundary faces of the mesh were fixed at room temperature (298 K), the large size of the mesh ensures that temperature gradients surrounding the melt pool are accurate. More details on the modeling approach and procedure are provided in Appendix A.

The material properties used to simulate weld pools of the Ni-base superalloy CMSX-4 are listed in Table 1. Several of these properties are taken directly from values produced in literature [21–23], while others were inputted as representative of Ni-base alloys. Two of these values were altered in order to produce calculated weld pool sizes and shapes that matched those observed from experimental welds. The effective thermal conductivity of liquid, found previously to be $0.0785 \text{ cal cm}^{-1} \text{ s}^{-1} \text{ K}^{-1}$ near the liquidus

temperature [22], was increased to $0.2 \text{ cal cm}^{-1} \text{ s}^{-1} \text{ K}^{-1}$. This modification can be justified, since temperatures in the weld pool can far exceed the liquidus temperature.

The processing parameters used to simulate both the laser and electron beam (EB) welds were similar. The beam radius was set to 0.75 mm, and the power distribution factor was set as 3.0. However, the differences in absorptivity from each type of beam are accounted for by setting the beam absorption coefficient to 0.6 for laser-beam welding and 1.0 for the EB weld simulations. Laser-beams with powers of 240, 360 and 500 W were simulated moving at travel speeds of 1, 6, 24 and 47 mm s^{-1} . Weld pools were also calculated under an EB power of 120, 180, 250, 500, 1000 and 1500 W moving at travel speeds of 1, 6, 24, 47, 75 and 95 mm s^{-1} . The radius and power distribution factors for each type of beam were held constant. The accuracy of the model was checked by comparing the computed and experimentally measured weld pool dimensions. No input parameter optimization was made directly to seek the agreement. However, the effective thermal conductivity and the effective viscosity values were guided by the previous research. In short, the previous correlations between the dimensionless heat input and effective viscosity and thermal conductivity developed in previous research were used [24].

The resulting data sets from the heat transfer and fluid flow calculations were used to map the microstructural development of across the entire solidification interface. A FORTRAN program was developed in order to calculate the local temperature gradient (G) and solidification velocity (V). The G values were calculated directly from the temperature data, and the solidification velocity was calculated using the geometric model developed by Rappaz et al. These calculations require knowledge of the weld pool shape, which was determined using the simulated temperature data. The shape determination was accomplished by utilizing the assumption that the vector with the maximum G will coincide with the normal to the solidification interface. The program carries out the following steps:

- (1) the liquidus temperature is located between individual grid spacings via linear interpolation;
- (2) temperature gradients in the liquid adjacent to this location are calculated along the three axes of the mesh, giving the quantities G_x , G_y and G_z ;
- (3) the temperature gradient normal to the solid–liquid interface is calculated, using the expression

$$G_{sl} = \sqrt{G_x^2 + G_y^2 + G_z^2};$$
- (4) the critical angles that describe the orientation of the local solid–liquid interface (θ_x , θ_y , θ_z) are calculated using the relationship $\theta_i = \cos^{-1}(G_i/G_{sl})$, where $i = x, y, z$;
- (5) the growth rate of the solid–liquid interface is calculated via $V_{sl} = S \cos \theta$, where S = heat source travel speed;
- (6) the ψ angles between the normal vector and the possible dendrite growth directions are calculated;

Table 1
CMSX-4 material properties used in finite-difference calculations.

Material property	Units	
Density of liquid	7.74	g cm^{-3}
Effective viscosity of liquid	3.0	$\text{g cm}^{-1} \text{ s}^{-1}$
Solidus temperature	1620	K
Liquidus temperature	1660	K
Enthalpy of solid at melting point	47.8	cal g^{-1}
Enthalpy of liquid at melting point	60	cal g^{-1}
Specific heat of solid	0.195	$\text{cal g}^{-1} \text{ K}^{-1}$
Specific heat of liquid	0.167	$\text{cal g}^{-1} \text{ K}^{-1}$
Thermal conductivity of solid	0.068	$\text{cal cm}^{-1} \text{ s}^{-1} \text{ K}^{-1}$
Effective thermal conductivity of liquid	0.2	$\text{cal cm}^{-1} \text{ s}^{-1} \text{ K}^{-1}$
Coefficient of thermal expansion	1.00×10^{-4}	K^{-1}
Emissivity of the material	0	
$d\gamma/dT$ of pure material	−1.37	$\text{dynes cm}^{-1} \text{ K}^{-1}$
Concentration of surface active species	0	wt. %
Surface excess at saturation	1.30×10^{-9}	mole cm^{-2}
Enthalpy of segregation	-3.97×10^4	cal mole^{-1}

- (7) the magnitude of these angles are used to determine which $\langle 1\ 0\ 0 \rangle$ growth variant will be operative at that location;
- (8) the temperature gradient parallel to the dendrite growth direction, G_{hkl} , is calculated using the equation $G_{hkl} = G_{sl} / \cos \psi$;
- (9) the dendrite growth velocity, V_{hkl} , is calculated using the equation $V_{hkl} = S \cos \theta / \cos \psi$.

2.2. Experimental

Modeling efforts were validated using a series of experimental weld trials on CMSX-4 substrates. The composition

Table 2
Composition of CMSX-4 (all values in wt.%).

	CMSX-4
Ni	Bal
C	0.002
Cr	6.36
Co	9.68
Mo	0.63
W	6.34
Ta	6.52
Ti	1
Al	5.62
B	0
Zr	0
Hf	0.1
Re	2.87

of the substrate is listed in Table 2. The surface upon which all welds were conducted was parallel to the $(0\ 0\ 1)$ crystal plane. Welds were conducted along the $[1\ 0\ 0]$, $[1\ 2\ 0]$ and $[1\ 1\ 0]$ directions. Laser welds were produced using a 750 W Nd:YAG laser operating at processing parameters equivalent to those used in weld pool simulations. EB welds were performed using a defocused beam and the processing parameters listed above. Weld cross-sections were prepared metallographically in order to measure the dimensions of the weld pool and the SX growth regions for comparison with the weld pool simulations and SX growth predictions. The SG area fraction was also measured for each weld condition via orientation imaging microscopy (OIM). Three weld cross-sections were measured to determine an average SG fraction, defined as the SG area (measured from OIM) divided by the fusion zone area (measured via optical microscopy).

3. Results

The accuracy of the weld pool simulations using the heat transfer and fluid flow code was judged based on its ability to replicate the experimental welds conducted on the SX substrates. Comparisons between actual and calculated weld pools were carried out by comparing two criteria: the pool dimensions (length, width and depth) and the pool shape. Fig. 2a shows a cross-sectional view of a simulated weld pool superimposed over the weld fusion zone produced by a laser pass performed with equivalent welding

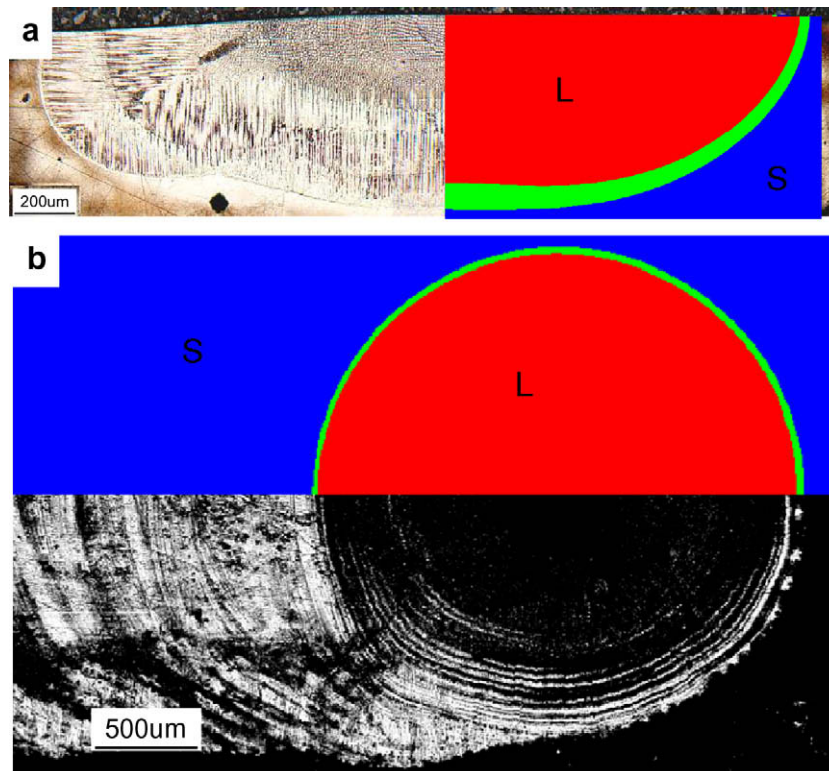


Fig. 2. Comparison of experimental and calculated weld pools for the $500\text{ W}-1\text{ mm s}^{-1}$ laser-weld condition, viewed (a) in cross-section and (b) along the substrate surface where the laser was shuttered.

parameters (500 W, 1 mm s⁻¹), while Fig. 2b displays a top-down view of the simulation in comparison to the weld surface that solidified moments after the laser was shuttered. Fig. 3 plots the calculated weld pool dimensions (length, depth and width) as a function of their experimentally measured counterparts for all laser-beam (Fig. 3a) and EB weld parameters (Fig. 3b) studied. Good agreement is shown for the laser-beam welds and for the EB welds prepared at powers at and below 500 W, but large deviations are present for the EB welds made at powers ≥ 1000 W.

Although the weld pool dimensions can easily be compared through direct measurement, assessment of the actual shape of the solid–liquid interface requires a more detailed analysis of the weld microstructures and simulations. The dendrite growth regions observed in a SX weld zone are a direct function of the weld pool shape. In light of this relationship, the dimensions of the crystal growth regions were used to parameterize the pool shape. The geometric model developed to describe the microstructural development of a SX weld was used to predict G_{hkl} and V_{hkl} (temperature gradient and solidification velocity parallel to the local dendrite growth direction) across the entire solidification interface. In order to do this, it is necessary to predict which $\langle 100 \rangle$ growth variant will be active by comparing the ψ angles between the $\langle 100 \rangle$ variants and the normal vector (the active growth variant will be that which possesses the smallest angle ψ). Fig. 4 illustrates the distribution of these growth regions for the simulated [1 0 0]–250 W–1.5 mm s⁻¹ EB weld. The three possible growth directions are indicated by color and are plotted across the entire solidification interface. Only half of the weld pool is shown, since symmetry is predicted across the weld centerline for this substrate orientation. The surface and centerline of the simulated melt pool are labeled in Fig. 4 as points of reference. For this example, the [1 0 0] dendrites grow parallel to the welding velocity at the weld crown, [0 0 1] dendrites grow vertically from the weld root, and [0 1 0] dendrites grow perpendicularly from the fusion line.

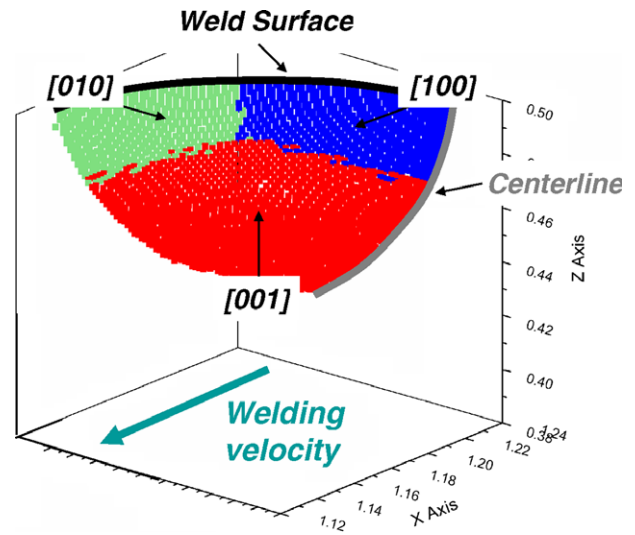


Fig. 4. Distribution of the $\langle 100 \rangle$ dendrite growth variants along the solid–liquid interface of the simulated [1 0 0]–250 W–1.5 mm s⁻¹ EB weld pool.

In order to validate these dendrite growth calculations, comparison was made between the predicted dendrite growth directions and the dendrite growth regions observed in the experimental weld structures. A direct comparison is given in Fig. 5, which superimposes the calculated dendrite growth direction predictions upon the corresponding measured growth directions (determined by OIM) for the [1 0 0]–240 W–1.5 mm s⁻¹ laser weld microstructure. Good agreement is shown in the span of each zone. Measurements were taken from multiple laser weld structures conducted in the (0 0 1)[1 0 0] orientation to verify that the weld pool shape was properly simulated over a wide range of welding conditions. Since the size of each dendrite growth zone is limited by the neighboring zones, the width and depth of the [1 0 0] zone was used to describe the weld pool shape. These values were measured from the low travel speed (1 and 6 mm s⁻¹) laser-beam welds, which contained signif-

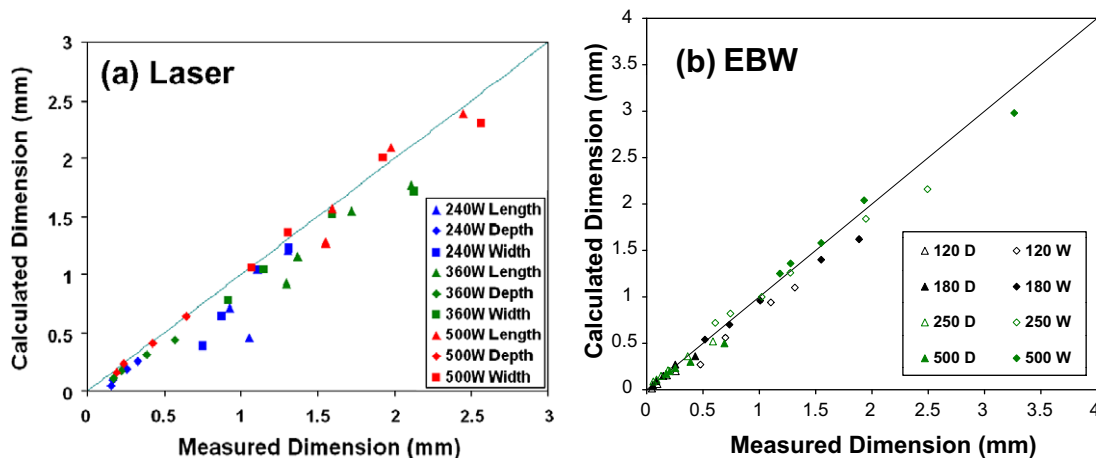


Fig. 3. Comparison of the experimental and calculated weld pool dimensions for all sets of welding parameters: (a) the length, depth and width of laser-beam welds and (b) the depth and width of EB welds.

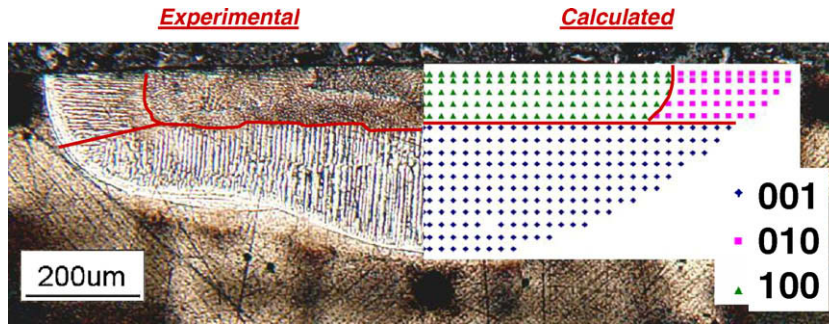


Fig. 5. The experimental and predicted dendrite growth regions for the [1 0 0]–240 W–1 mm s⁻¹ laser-weld condition.

icant [1 0 0] dendrite zones. The equivalent dimensions of the calculated [1 0 0] growth region, as predicted by the geometric model, were also collected. The width and depth of the experimental and calculated [1 0 0] zones are compared in Fig. 6a and b, respectively, for several laser powers at travel speeds of 1 and 6 mm s⁻¹. Good agreement is shown for both parameters over all conditions.

The geometric model developed to describe the microstructural development of a SX weld was used to predict G_{hkl} and V_{hkl} across the entire solidification interface. As a majority of the experimental SX welds conducted in this study were of the [1 0 0]|| (0 0 1) orientation, the calculated G_{hkl} and V_{hkl} fields presented herein will utilize the same weld/substrate orientation relationship. The equations for calculating G_{hkl} and V_{hkl} for this orientation values are presented in Table 3. The ramifications of SX growth on the distribution of G and V across the entire solidification interface for the [1 0 0]–250 W–1.5 mm s⁻¹ simulated EB weld are illustrated in Figs. 7 and 8, respectively. The data is presented across the same three-dimensional representation of the weld pool as shown in Fig. 4. The distribution of G_{sl} and G_{hkl} are compared in Fig. 7a and b. The same relationships are shown for solidification velocity in Fig. 8. The growth rate of the solidification interface V_{sl} is described in Fig. 8a, while the dendrite tip velocity for the case of SX growth is described in Fig. 8b. (Note that

Table 3

Calculations for G_{hkl} and V_{hkl} for the [1 0 0]|| (0 0 1) crystal orientation.

	Condition	V_{hkl}	G_{hkl}
[1 0 0]	$\psi_x < \psi_y, \psi_z$	$V_{sl}/\cos \psi_x (=S)$	G_x
[0 1 0]	$\psi_y < \psi_x, \psi_z$	$V_{sl}/\cos \psi_y$	G_y
[0 0 1]	$\psi_z < \psi_x, \psi_y$	$V_{sl}/\cos \psi_z$	G_z

the color scales evolve from low values in red to high values in blue.)

4. Discussion

4.1. Heat transfer and fluid flow

As shown in Fig. 3, the heat transfer and fluid flow calculations accurately capture the weld pool dimensions for the laser and EB welds for powers up to 500 W. Many of the welds were observed to exhibit wide and shallow pools, which is attributed largely due to the flow of liquid from under the heat source outward to the edge of the pool. This flow direction is caused by a negative gradient in surface tension with temperature ($d\gamma/dT$), confirmed experimentally as $-1.37 \text{ dynes cm}^{-1} \text{ K}^{-1}$ in Ref. [15]. Significant deviation between calculated and experimental dimensions were observed for EB welds made at powers of 1000 and 1500 W. The experimental EB weld depths were signifi-

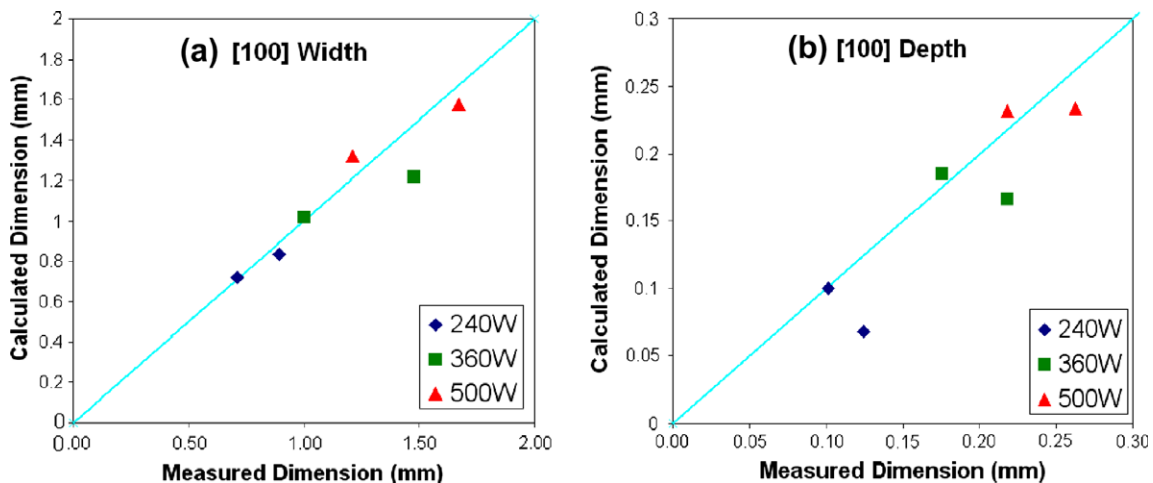


Fig. 6. Comparison of the experimental and calculated dimensions of the [1 0 0] dendrite growth zone: (a) width and (b) depth.

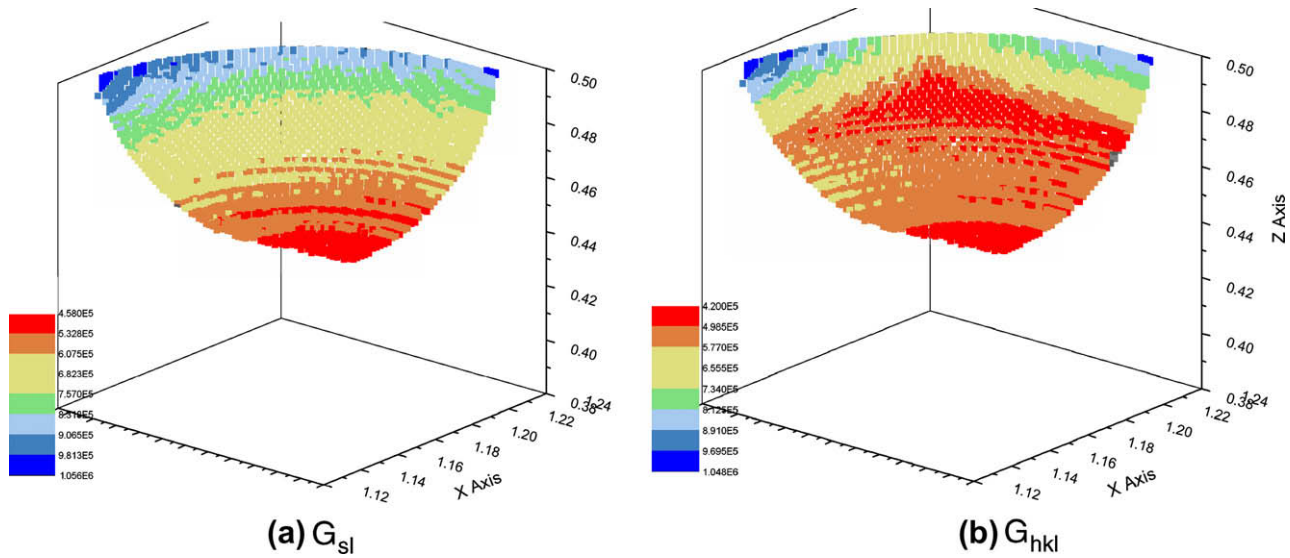


Fig. 7. Comparison of the temperature gradient distribution (in $K m^{-1}$) along the solid–liquid interface of the simulated $250 W-1.5 mm s^{-1}$ weld pool for (a) G_{sl} , the temperature gradient normal to the solid–liquid interface and (b) G_{hkl} , the temperature gradient parallel to dendrite growth for a $[1 0 0]|| (0 0 1)$ welding orientation on SX substrate.

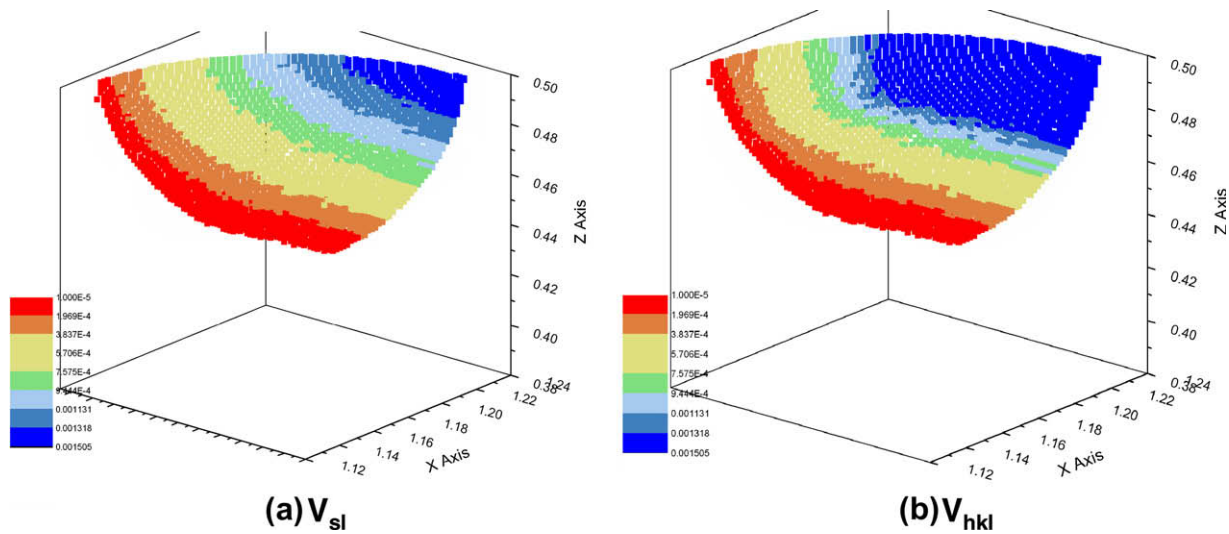


Fig. 8. Comparison of the dendrite solidification velocity distribution (in $m s^{-1}$) along the solid–liquid interface of the simulated $250 W-1.5 mm s^{-1}$ weld pool for (a) V_{sl} , the growth rate of the solid–liquid interface and (b) V_{hkl} , the dendrite tip velocity for a $[1 0 0]|| (0 0 1)$ welding orientation on SX substrate.

cantly greater than that predicted in simulation. The cause for this discrepancy is the initiation of keyhole mode of energy transfer at EB powers $\geq 1000 W$. The particular heat transfer and fluid flow code used in this study was not developed for predicting this mode of heat transfer. The keyhole mode was effectively avoided at the lower beam powers by underfocusing the beam, which produced shallow pool shapes similar to those observed under the laser-beam. Because of the appearance of keyhole-type welds was not replicated in simulation, the calculated temperature fields would not serve as effective inputs for predicting the CET. In addition, as described in more detail below, these high-power conditions lead to undesirably

high levels of SGs. Hence, these high-power welds were omitted from the remainder of the modeling effort.

The weld pool shapes were also accurately predicted for both laser and EB weld trials. Fig. 6 shows good conformity between the measured and predicted dimensions of the $[1 0 0]$ dendritic zone. The results can be taken as an indication that the experimental weld pool shapes were accurately rendered by the heat transfer and fluid flow code. This good agreement was provided by increasing the effective viscosity of the liquid from the previously measured value of $0.0979 g cm^{-1} s^{-1}$ [22] up to $3.0 g cm^{-1} s^{-1}$. This alteration increases the slope of the edges of the weld pool, allowing the $[1 0 0]$ dendrites to be active at deeper

pool depths. Since the thermal properties of a Ni-base superalloy are isotropic at the scale of fusion welding [7], the assumption is made that the pool shapes for welds conducted along the $[1\ 1\ 0]$ and $[1\ 2\ 0]$ crystal directions were equivalent.

4.2. Single-crystal development

The case of SX growth significantly alters the magnitudes and distributions of G_{hkl} and V_{hkl} across the solid–liquid interface due to the restrictions of dendrite growth along the $\langle 1\ 0\ 0 \rangle$ crystal directions. The map of G_{sl} shown in Fig. 7a indicates that heat flow was greatest at the surface of the weld pool (in blue) and lowest at the weld root (in red). This distribution is consistent with higher convective heat transfer near the surface than near the weld root. The effects of fluid flow within the liquid have clearly impacted the temperature fields within the pool. In this case, the convergence of fluid currents from the pool surface to the weld root induce higher temperatures in the liquid in this location, causing the relatively low temperature gradients at the weld root. In addition, the application of SX weld development restrictions causes this region of low G to expand further along the solid–liquid interface. Solidification in this region occurs vertically along the $[0\ 0\ 1]$ crystal direction. By comparing the data from Fig. 7b with the dendrite growth directions in Fig. 4, it is shown that the low G_{hkl} (in red) spans the entire $[0\ 0\ 1]$ zone right up to the junctions with the $[1\ 0\ 0]$ and $[0\ 1\ 0]$ growth regions. This decrease in G up to the dendrite junctions is caused by the steady increase in the ψ angle. Because the dendrite growth direction deviates from the solid–liquid interface normal, the direction of maximum heat flow direction will not coincide with the dendritic axis. This effect causes $G_{hkl} \leq G_{sl}$. The effect is most pronounced at the dendrite growth junctions, where ψ is greatest. Moreover, the position of low G_{hkl} (in red) in the middle of

the pool corresponds to the point at which all three growth regions converge. The importance of the dendrite growth junctions is illustrated in Fig. 9a, which plots the magnitudes of G_{sl} and G_{hkl} as a function of depth along the weld centerline. G_{hkl} is always less than G_{sl} , and G_{hkl} reaches a minimum precisely at the location where the $[0\ 0\ 1]$ and $[1\ 0\ 0]$ dendrites meet.

The calculated growth rates in Fig. 8 show that SX growth mechanics also affect the distribution of solidification velocity. The growth rate of the solid–liquid interface V_{sl} increases monotonically from the weld root to the weld crown. This is caused by the curvature of the interface; regions in which the angle θ is lower grow at a faster rate. SX growth does not counteract this trend, but it will affect the magnitudes of the dendrite tip velocities throughout the weld pool. For the $[1\ 0\ 0]||[0\ 0\ 1]$ orientation, all dendrites in the $[1\ 0\ 0]$ zone solidify at the same rate, equal to the travel speed. This is a result of the dendrites being parallel to the travel speed, and hence $\theta = \psi$. The constant V_{hkl} in the $[1\ 0\ 0]$ zone is also shown in Fig. 9b, which plots V_{hkl} and V_{sl} as a function of weld pool depth along the weld centerline. This plot also illustrates that $V_{hkl} \geq V_{sl}$ along the entire solid–liquid interface. Because SX growth restricts the dendrite growth directions to the $\langle 1\ 0\ 0 \rangle$ variants, the range of G and V which will determine the degree of constitutional supercooling (CS) along any point of the solid–liquid interface will be altered. Fig. 9 shows that $G_{hkl} \leq G_{sl}$ and $V_{hkl} \geq V_{sl}$. The degree of CS is modified, and $G_{hkl}/V_{hkl} \ll G_{sl}/V_{sl}$. Thus, the nucleation of equiaxed grains in the liquid is actually promoted by SX development characteristics.

4.3. Stray grain formation

The calculated local G_{hkl} and V_{hkl} data serve as indicators of the tendency to form SGs at any point along the solidifying solid–liquid interface. By collecting all of the

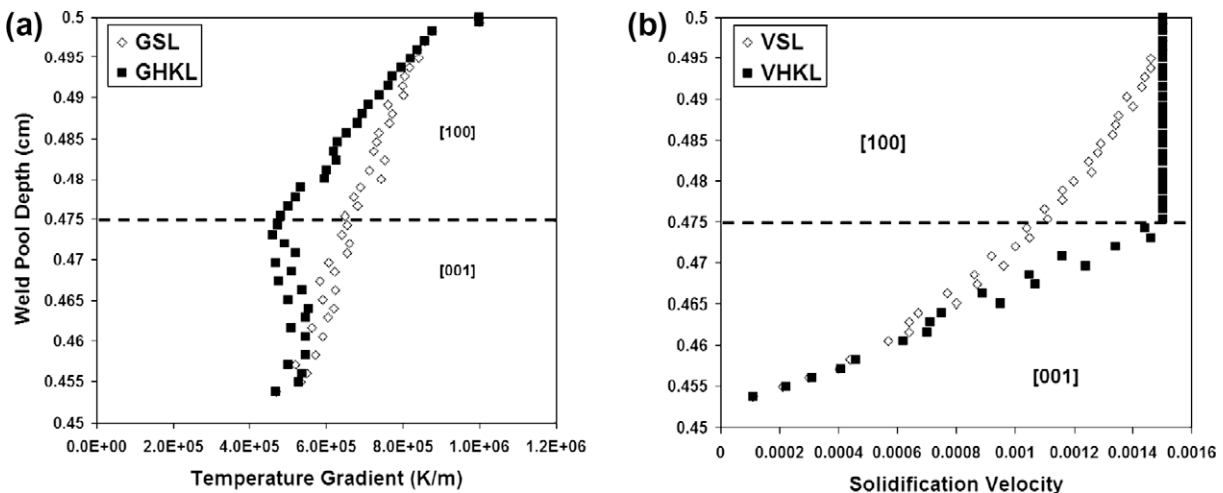


Fig. 9. Comparison of the magnitudes of the solidification parameters along the weld centerline under polycrystalline and SX $[1\ 0\ 0]||[0\ 0\ 1]$ growth conditions: (a) temperature gradient and (b) solidification velocity.

solidification parameter data from the entire solid–liquid interface, predictions can be made about the fraction of SGs that nucleate in the weld pool. The procedure used in this research followed that of Vitek [10]. Eq. (2) was rearranged to give the SG fraction ϕ as a function of G and V :

$$\phi = 1 - \exp \left\{ \frac{-4\pi N_o}{3} \left(\frac{1}{(n+1)(G^n/aV)^{1/n}} \right)^3 \right\}$$

$$= -2.356 \times 10^{19} \left(\frac{V}{G^{3.4}} \right)^{3/3.4} \quad (4)$$

The simplified equation on the right assumes the same material constants used by Vitek: $a = 1.25 \times 10^6 \text{ K}^n \text{ m}^{-1} \text{ s}^{-1}$, $n = 3.4$, $N_o = 2 \times 10^{14} \text{ m}^{-3}$. ϕ was calculated along each point of the solid–liquid interface using the calculated G_{hkl} and V_{hkl} as inputs. As an example, two ϕ maps are presented in Fig. 10. The 250 W–95 mm s⁻¹ map (Fig. 10a) represents a low heat input condition, and the 500 W–6 mm s⁻¹ map (Fig. 10b) signifies a weld with high heat input. The range of ϕ shown in each map indicates the overall SG formation characteristics for each condition. The low heat input generates a wide range of ϕ , which only reaches unity at the weld crown. Conversely, a majority of the solid–liquid interface has $\phi = 1$ under a high heat input. Thus, low-power/high-travel-speed conditions are useful for helping to avoid SG formation and preserve SX solidification. Such generalizations about the effects of welding parameters on SG formation can be expanded by calculating the SG volume fraction for the entire weld pool.

The overall SG formation behavior for the full weld can be expressed by determining the area-weighted average ϕ across the entire solid–liquid interface:

$$\Phi = \frac{\sum_i A_i \phi_i}{\sum_i A_i} \quad (5)$$

where A and ϕ are the area of a solid–liquid interface and SG area fraction for a particular location i . Since Φ takes into account the entire solidification front, it is more indicative of SG formation than G/V , which varies throughout the weld pool. This value was calculated for each of the laser and EB welding conditions. The data is presented as a function of welding parameters in Fig. 11.

The 1000 and 1500 W EB data are omitted, as those weld pool simulations did not accurately represent the experimental welds. The results show the significant effects that welding parameters will have on SG formation. The Φ data in Fig. 11 illustrates the negative effect that beam power will have on SG formation. The heightened beam power lowers G throughout the weld pool and promotes the nucleation of equiaxed grains. The effect of travel speed is more complex. For powers ≤ 250 W, SG formation is generally observed to reach a maximum at an intermediate travel speeds. When P is high (≥ 500 W EB), SG formation always decreases as the travel speed increases. The transition in behavior has been observed in other work [10] and can be explained based on the relative increases in temperature gradient and growth rate with changes in travel speed. When the travel speed is low, initial increases in the speed will cause an increase in the growth rate with only minor changes in the temperature gradient. As a result, G/V generally decreases, and the amount of SGs will therefore increase. Further increases in the travel speed will induce larger increases in the temperature gradient, and, according to Eqs. (3) and (4), G has a larger effect on SG formation than V . Thus, SG formation will subsequently decrease with further increases in the travel speed. Vitek performed a theoretical analysis [10] of the effects of solidification parameters on ϕ . His results were similar to those presented here in which decreases in power and increases in travel speed were generally beneficial. His results also demonstrated a transition in behavior for the same alloy at a similar travel speed of $\sim 14 \text{ mm s}^{-1}$.

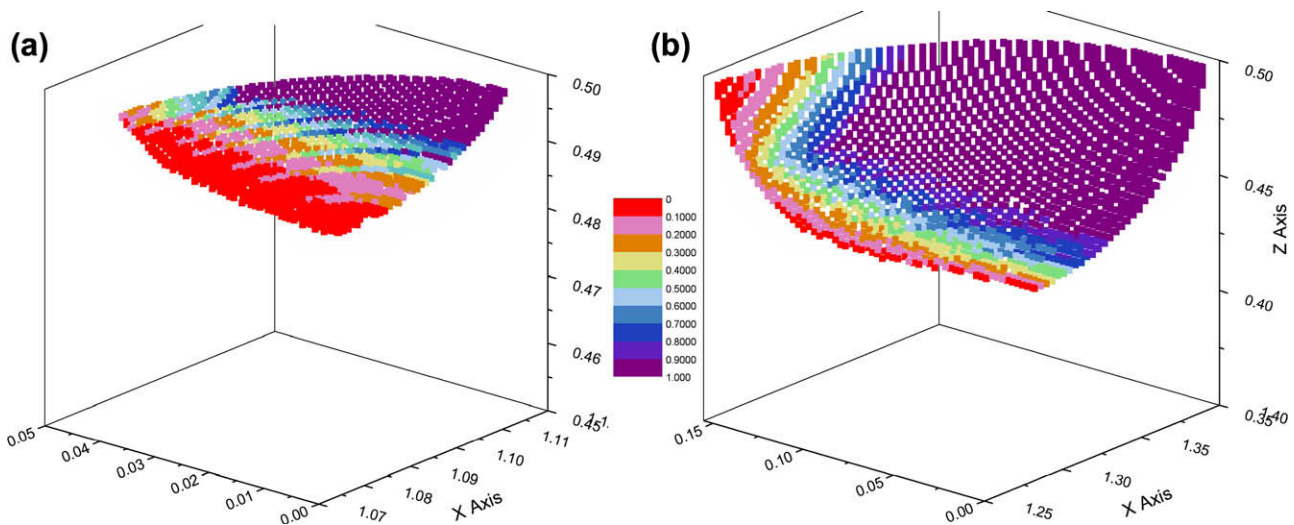


Fig. 10. The predicted SG volume fraction parameter f along the solid–liquid interface of simulated weld pools for the (a) [100]–250 W–95 mm s⁻¹ and (b) [1 0 0]–500 W–6 mm s⁻¹ conditions.

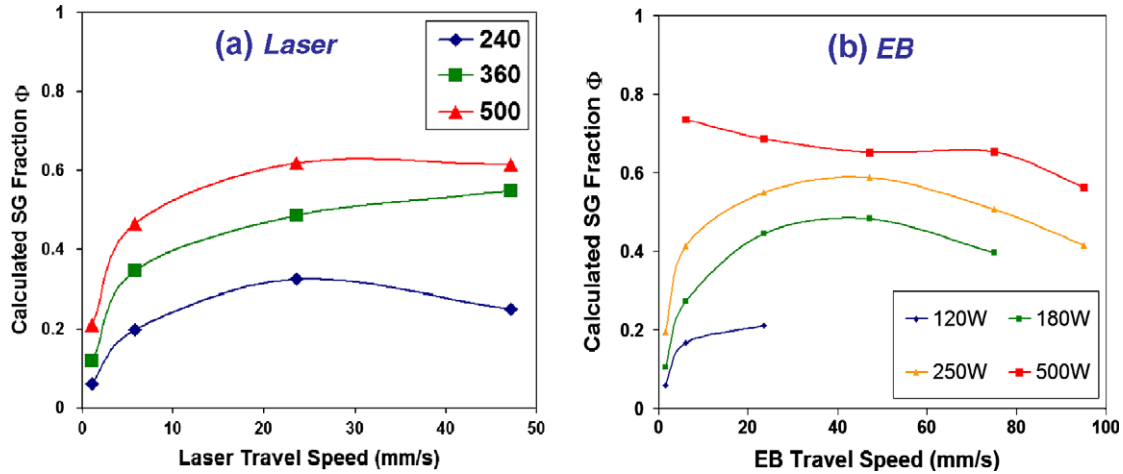


Fig. 11. The effect of welding parameters on the predicted SG volume fraction within simulated (a) laser-beam and (b) EB weld pools for the [1 0 0]||[0 0 1] substrate orientation.

Fig. 12 shows the experimental measurements of SG fraction as a function of welding parameters. The experimental data shows similarities to the SG predictions made from weld pool simulations. The effect of increasing power is shown in the EB weld data in Fig. 12b. The 1000 and 1500 W data contained greater SG fractions at every travel speed. Both sets of experimental data reveal a maximum SG fraction at an intermediate travel speed of $\sim 6 \text{ mm s}^{-1}$. Although the magnitudes of the predicted SG fractions are not accurate, the general effects of power and travel speed on SG formation are captured by the model.

4.4. Parameter optimization

The calculated SG contents shown in Fig. 11 were produced with the material constants and nuclei density determined by Gaumann et al. [9]. In that work, the material constants \mathbf{a} and \mathbf{n} were chosen in order to make the resulting CET boundary closely match previous calculations conducted using rapid solidification models. The nuclei density N_o was determined by fitting experimental SG data

to the calculated solidification conditions in the weld pool. The solidification conditions for the weld pool were represented using an average value of G^m/V (calculated using the Rosenthal solution for conduction only) for six sets of welding parameters. Assuming that the values of G and V determined here are more accurate due to the more advanced heat/fluid flow model used, and considering that a wide range of experimental conditions have been investigated, an opportunity exists to potentially improve the accuracy of the values of \mathbf{a} , \mathbf{n} and N_o . In order to optimize these values, a parameter δ was defined which describes the overall deviation between the experimental and calculated SG fractions:

$$\delta = \sum_i (\Phi_{exp} - \Phi_{calc})^2 \tag{6}$$

If the calculated SG fraction perfectly matched the experimental SG content for all welding conditions, $\delta = 0$. When using the constants defined by Gaumann, $\delta = 3.74$. The parameter optimization procedure was carried out in the following manner:

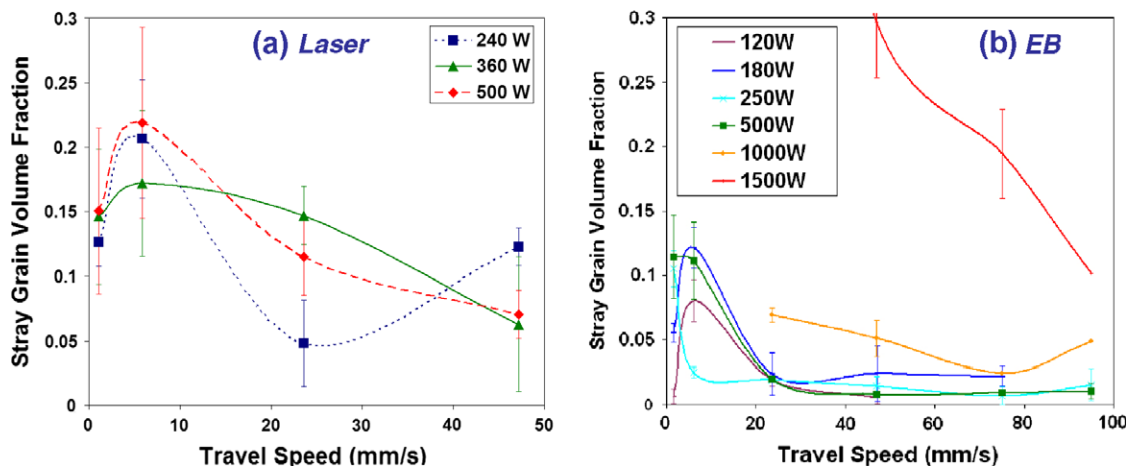


Fig. 12. The effect of welding parameters on SG volume fraction within the experimental (a) laser-beam and (b) EB weld structures for the [1 0 0]||[0 0 1] substrate orientation.

Table 4
The original and optimized parameters for the calculation of SG volume fraction.

	Original	Optimized
N_o (m^{-3})	2×10^{15}	1.18×10^{15}
a ($\text{K}^n \text{m}^{-1} \text{s}^{-1}$)	1.25×10^6	2.03×10^6
n	3.4	5.3

- (1) the optimized N_o (which makes $\Phi_{exp} = \Phi_{calc}$) was calculated for each weld condition;
- (2) the average N_o was calculated and applied to the Φ calculations for each weld condition;
- (3) the δ parameter was recalculated in order to observe the global deviations between calculated and experimental Φ ;
- (4) the process was repeated iteratively for the \mathbf{a} and \mathbf{n} constants using the updated value of N_o .

The procedure was repeated twice for each constant, after which the values did not change significantly. The original and optimized values for each constant are listed in Table 4. The new values of N_o , \mathbf{a} and \mathbf{n} resulted in predictions of SG content that were more closely aligned with the experimental values. In this way, the final calculated δ parameter was reduced from 3.74 to 0.08. The parameter-optimized calculated Φ values are plotted in Fig. 13. Reasonable agreement is obtained between the experimental and calculated magnitudes of Φ , particularly with the low-power, high-travel-speed data. While the SG peak experimentally observed at $\sim 6 \text{ mm s}^{-1}$ is now offset to higher travel speeds, the general phenomenon of a maximum Φ at an intermediate speeds is predicted. The optimized data also implies that there will be a critical beam power (500 W) at which the SG fraction will increase sharply at all values of S . The same behavior is demonstrated by the experimental EB weld data, albeit for a higher P (1000 W).

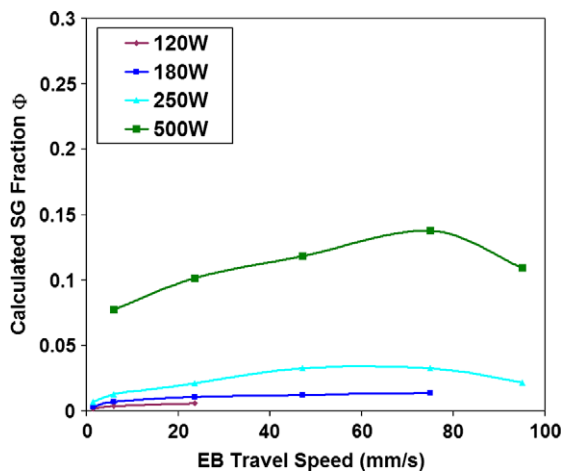


Fig. 13. The calculated SG volume fraction F as a function of EB welding parameters using the optimized material constants.

5. Conclusions

The formation of SGs in SX alloy CMSX-4 was investigated by combining three types of simulations: a heat transfer and fluid flow code to simulate the weld pool size and shape and the temperature profiles in three dimensions as a function of welding parameters; a SX development model to determine the solidification parameters along the dendrite growth direction; and a model which predicts SG formation as a function of material properties and solidification parameters. The following conclusions can be drawn from this work:

- (1) Good agreement between measured and calculated pool sizes, shapes and growth regimes have been observed for welds made at beam powers up to 500 W.
- (2) At a fixed power, SG content initially increases and then decreases with increasing travel speed. Increases in beam power generally produce an increase in the SG content.
- (3) The restriction of $\langle 100 \rangle$ growth directions in the pool significantly changes the magnitudes of G and V along the growth direction relative to those normal to the solid–liquid interface. In particular, the magnitude of G decreases and V increases along the dendrite growth direction (relative to the solidification interface normal). The temperature gradient tends to be the lowest at intersections between various dendrite growth regimes because the growth direction deviates the most from the solidification interface normal at these locations. These factors tend to promote SG formation in the pool.
- (4) Revised values of N_o , \mathbf{a} and \mathbf{n} for CMSX-4 have been proposed that provide reasonable agreement between the measured and calculated values of SG content over a wide range of welding parameters.

Acknowledgements

The authors would like to acknowledge the financial support of the National Science Foundation through Grant No. 0500254. The SX substrates used for welding trials were cast by the Howmet Corporation, a division of Alcoa, Inc. The EB welding experiments were made possible by the assistance of Paul Burgardt and Thomas Lienert of Los Alamos National Laboratories.

Appendix A. Heat transfer and fluid flow simulation

The liquid metal velocities in the weld pool were computed assuming steady state since the weld cross-section does not change with time except at the beginning and the end of welding and constant density following Boussinesq's approximation. A moving Cartesian co-ordinate system where the heat source moves at a constant welding speed, U , in the negative

x -direction, was adapted. Under these conditions, the momentum conservation equations can be written as [25]:

$$\rho \frac{\partial(u_i u_j)}{\partial x_i} = \frac{\partial}{\partial x_i} \left(\mu \frac{\partial u_j}{\partial x_i} \right) - \rho U \frac{\partial u_j}{\partial x_1} - \frac{\partial p}{\partial x_j} + \rho g_j \beta (T - T_r) + S_j \quad (\text{A1})$$

where ρ is the density, x_i is the distance along the $i = 1, 2$ and 3 (same as x, y and z) directions, u is the velocity in the direction of its subscript, μ is the effective viscosity, p is local pressure minus the hydrostatic pressure, g_j is the gravitational acceleration, β is the coefficient of volume expansion, T is temperature, T_r is the reference temperature and S_j is the source term given as:

$$S_j = -c_m \left(\frac{(1 - f_L)^2}{f_L^3} \right) u_j + \frac{\partial}{\partial x_i} \left(\mu \frac{\partial u_i}{\partial x_j} \right) \quad (\text{A2})$$

where f_L is the liquid fraction, c_m is a constant that takes into account mushy zone morphology. The first term on the right-hand side represents the frictional dissipation in the mushy zone according to the Carman–Kozeny equation for flow through a porous media [26]. The value of the effective viscosity in Eq. (A1) is a property of the specific welding system which is much higher than that of the molecular viscosity of the metal. The higher value allows accurate modeling of the high rates of transport of momentum in systems with strong fluctuating velocities in small weld pools [27]. The pressure field was obtained by solving the following continuity equation simultaneously with the momentum equation:

$$\frac{\partial(\rho u_i)}{\partial x_i} = 0 \quad (\text{A3})$$

The enthalpy H is represented by a sum of sensible heat h and latent heat content ΔH , i.e., $H = h + \Delta H$, where $h = \int C_p dT$, C_p is the specific heat, $\Delta H = f_L L$, L is the latent heat of fusion and the liquid fraction, f_L , in the mushy zone is assumed to vary linearly with temperature.

The steady state transport of heat in the weld workpiece can be expressed by the following modified energy equation:

$$\rho \frac{\partial(u_i h)}{\partial x_i} = \frac{\partial}{\partial x_i} \left(\frac{k}{C_p} \frac{\partial h}{\partial x_i} \right) - \rho \frac{\partial(u_i \Delta H)}{\partial x_i} - \rho U \frac{\partial h}{\partial x_1} - \rho U \frac{\partial(\Delta H)}{\partial x_1} \quad (\text{A4})$$

where k is the thermal conductivity. In the liquid region, the value of the thermal conductivity in Eq. (A4) is taken as the effective thermal conductivity which is a property of the specific welding system and is much higher than the thermal conductivity of the liquid. The higher value allows accurate modeling of the high rates of transport of heat in systems with strong fluctuating velocities in the weld pool [27]. Since the weld is symmetrical about the weld center line only half of the workpiece is considered and gradients of all variables are taken as zero. At the top surface the velocity boundary conditions for the horizontal components of velocity, u and v , are obtained by

Marangoni boundary conditions given by Eqs. (A5a) and (A5b). Furthermore since there is no normal velocity on the weld pool surface, the vertical component of velocity, w is zero as indicated in Eq. (A6).

$$\mu \frac{\partial u}{\partial z} = f_L \frac{d\gamma}{dT} \frac{\partial T}{\partial x} \quad (\text{A5a})$$

$$\mu \frac{\partial v}{\partial z} = f_L \frac{d\gamma}{dT} \frac{\partial T}{\partial y} \quad (\text{A5b})$$

$$w = 0 \quad (\text{A5c})$$

where $d\gamma/dT$ is the temperature coefficient of surface tension. The heat flux at the top surface is given as:

$$k \frac{\partial T}{\partial z} = \frac{dQ\eta}{\pi r_b^2} \exp\left(-\frac{d(x^2 + y^2)}{r_b^2}\right) - \sigma \varepsilon (T^4 - T_a^4) - h_c (T - T_a) \quad (\text{A6})$$

where r_b is the arc radius, d is the arc power distribution factor, Q is the total power, η is the absorptivity, σ is the Stefan–Boltzmann constant, h_c is the heat transfer coefficient, and T_a is the ambient temperature. The first term on the right-hand side is the heat input from the Gaussian heat source. The second and third terms represent the heat loss by radiation and convection, respectively. At all other surfaces, temperatures are set at ambient temperature and all velocities are set to zero.

The governing equations were discretized in the following form using a control volume method involving non-uniform fixed grids and solved numerically [25]:

$$a_P \phi_P = \sum_{nb} (a_{nb} \phi_{nb}) + S_U \Delta V \quad (\text{A7})$$

where ϕ is a general variable such as velocity or enthalpy, a is the coefficient of the variable, the subscript P represents a given grid point, the subscript nb indicates the neighbors of the given grid point P , and ΔV is the control volume. The coefficient a_P is defined as:

$$a_P = \sum_{nb} a_{nb} - S_P \Delta V \quad (\text{A8})$$

The terms S_U and S_P are used in the source term linearization as:

$$S = S_U + S_P \phi_P \quad (\text{A9})$$

The system of equations expressed by Eq. (A8) were solved by a Gaussian elimination technique known as tridiagonal matrix algorithm (TDMA) [25]. Scalar grid points were located at the center of each control volume, whereas the velocity components were staggered with respect to scalar locations to achieve improved stability and rapid convergence of numerical calculations. The discretized equations were solved using SIMPLE algorithm [25]. using constant thermophysical properties and typically $112 \times 62 \times 77$ grids to make the calculations tractable and accurate.

Two convergence criteria were used, i.e., residuals and heat balance. The residuals for velocities and enthalpy were defined as:

$$R = \frac{\sum_{domain} \left| \frac{\sum_{nb} (a_{nb} \phi_{nb}) + S_U \Delta V}{a_P} - \phi_P \right|}{\sum_{domain} |\phi_P|} \quad (\text{A10})$$

Converged solution was assumed when the residual, R , for each variable were very small, typically 10^{-4} . In addition, the following overall heat balance had to be satisfied:

$$\theta = \frac{|\text{net heat input}|}{|\text{total heat out}|} \quad (\text{A11})$$

Convergence was assumed when $R \leq 10^{-4}$ and $0.99 \leq \theta \leq 1.01$. More strict convergence criteria do not change the final results but increase computational time.

References

- [1] Harris K, Erickson GL, Sikkenga SL, Brentnall WD, Aurrecochea JM, Kubarych KG. Development of the rhenium containing superalloys CMSX-4 and CM-186LC for single crystal blade and directionally solidified vane applications in advanced turbine engines. *Superalloys* 1992;297–306.
- [2] Webber J. Power industry experiences surge in welding research. *Weld J* 2003;82:40–3.
- [3] Gallardo J, Rodriguez J, Herrera E. *Wear* 2002;252:264–8.
- [4] Hunt J. *Mater Sci Eng* 1984;65:75–83.
- [5] Rappaz M, David SA, Vitek JM, Boatner LA. *Metall Mater Trans A* 1989;20:1125–38.
- [6] David SA, Vitek JM, Rappaz M, Boatner LA. *Metall Mater Trans A* 1990;21:1753–66.
- [7] Rappaz M, David SA, Vitek JM, Boatner LA. *Metall Mater Trans A* 1990;21:1767–82.
- [8] Gaumann M, Trivedi R, Kurz W. *Mater Sci Eng A* 1997;226–228:763–9.
- [9] Gaumann M, Bezencon C, Canalis P, Kurz W. *Acta Mater* 2001;49:1051–62.
- [10] Vitek JM. *Acta Mater* 2005;53:53–67.
- [11] Rosenthal D. *Trans ASME* 1946;68:849–66.
- [12] Yoshihiro F, Saida K, Nishimoto K. *Mater Sci Forum* 2006;512(5):313–8.
- [13] Park JW, Babu SS, Vitek JM, Kenik EA, David SA. *J Appl Phys* 2003;94(6):4203–9.
- [14] Park JW, Vitek JM, Babu SS, David SA. *Sci Technol Weld Join* 2004;9(6):472–82.
- [15] Liu W, DuPont JN. *Acta Mater* 2004;52:4833–47.
- [16] Liu W, DuPont JN. *Acta Mater* 2005;53(5):1545–58.
- [17] Anderson TD, DuPont JN, DebRoy T. *Metall Mater Trans A*, accepted for publication.
- [18] Anderson TD, DuPont JN. Stray grain formation and solidification cracking susceptibility of single crystal Ni-base superalloy CMSX-4. *Weld J*, accepted for publication.
- [19] Mundra K, DebRoy T, Kelkar K. *Numer Heat Transfer, Part A Applications* 1996;29(2):115–29.
- [20] Zhang W, Kim CL, DebRoy T. *J Appl Phys* 2004;95:5210–9.
- [21] Li Z, Mills K, McLean M, Mukai K. *Metall Mater Trans B* 2005;36:247–54.
- [22] Aune R. Thermophysical properties of IN738LC, MM247LC and CMSX-4 in the liquid and high temperature solid phase. *Superalloys 718, 625, 706 and Derivatives*, ASM International, Materials Park, Ohio; 2005. p. 467–76.
- [23] Hayashi M, Jakobsson A, Tanaka T, Seetharaman S. *High Temp High Press* 2004;35–36:441–5.
- [24] De A, DebRoy T. *J Appl Phys* 2004;95(9):5230–9.
- [25] Patankar SV. *Numerical heat transfer and fluid flow*. New York: Hemisphere Publishing Corporation; 1982.
- [26] Brent AD, Voller VR, Reid KJ. *Numer Heat Transfer* 1988;13:297–318.
- [27] DebRoy T, Majumdar AK. *J Metals* 1981;33(11):42–7.